J. Fluid Mech. (2012), *vol.* 706, *pp.* 295–322.
doi:10.1017/jfm.2012.254

Acoustic and hydrodynamic analysis of the flow around an aerofoil with trailing-edge serrations

L. E. Jones† and R. D. Sandberg

Aerodynamics and Flight Mechanics Research Group, School of Engineering Sciences, University of Southampton, Southampton SO17 1BJ, UK

(Received 22 September 2011; revised 23 March 2012; accepted 24 May 2012; first published online 6 July 2012)

Direct numerical simulations of the flow around a NACA-0012 aerofoil are conducted, employing an immersed boundary method to represent flat-plate trailing-edge extensions both with and without serrations. Properties of the turbulent boundary layer convecting over the trailing edge are similar for both cases. For cases with serrations, the trailing-edge noise produced by the flow over the aerofoil is observed to decrease in amplitude, and the frequency interval over which the noise reduction occurs differs depending on the serration length. The directivity and spanwise coherence of the trailing-edge noise appears largely unaffected by the serrations. The hydrodynamic behaviour in the vicinity of the trailing-edge extensions is investigated. The streamwise discontinuity imparted upon the turbulent flow by the straight trailing edge can clearly be observed in statistical quantities, whereas for the serrated case no spanwise homogeneous discontinuities are observed. The trailing-edge serrations appear to break up the larger turbulent structures convecting into the wake, and to promote the development of horseshoe vortices originating at the serrations themselves.

Key words: aeroacoustics, noise control, turbulent boundary layers

1. Introduction

When considering aerofoil self-noise it is typical for studies to focus primarily upon trailing-edge noise. Brooks, Pope & Marcolini (1989) classified five mechanisms for aerofoil self-noise, for which all but one (noise generated via the wing-tip vortex) are generated by disturbance interaction with the aerofoil trailing edge. Turbulent fluctuations in the vicinity of a sharp edge of a solid body scatter more efficiently at low Mach numbers than fluctuations in free space (M^5: cf. M^8 in Lighthill 1952 and Ffowcs Williams & Hall 1970), and hence trailing-edge noise is increasingly significant at low Mach numbers. It is apparent, then, that in order to reduce total aerofoil noise further, trailing-edge noise must be considered. Howe (1991) performed a numerical analysis of a flat plate, with the trailing edge modified by the presence of serrations possessing a sawtooth profile. Howe predicted that the intensity of radiation at the trailing edge could be reduced by such a modification, with the magnitude of the reduction depending on the length and spanwise spacing of the teeth, and the frequency of the radiation. It was determined that the dimensions of an individual serration should be at least of the order of the turbulent boundary layer thickness, and that longer, narrower teeth should yield a greater intensity reduction. Oerlemans *et al.* (2009) investigated experimentally the effect of adding trailing-edge serrations,

† Email address for correspondence: ljones@soton.ac.uk

as well as optimizing aerofoil geometry, to full size wind-turbine blades. It was found that for realistic aerofoil geometries overall self-noise reductions of 2–3 dB are possible without adversely affecting aerodynamic performance. Nevertheless, the reduction in self-noise amplitude was found to be most significant at lower frequencies, and the effect became more pronounced with increasing wind velocity. It appears that applying serrations to the aerofoil trailing edge is a valid means of reducing aerofoil self-noise without compromising aerodynamic performance. The mechanism by which this noise reduction occurs is not yet known. The addition of brushes to aerofoil trailing edges has also been found to reduce the intensity of trailing-edge noise (Herr & Dobrzynski 2005), although the mechanism for noise reduction in that case is likely due to the increased compliancy of the brushes weakening the diffraction effect at the aerofoil trailing edge. Geometrical modifications similar to trailing-edge serrations, termed 'chevrons', have been applied to jet nozzles and found to reduce the associated jet noise (Callender, Gutmark & Martens 2005). However, although jet nozzle chevrons may appear visually similar to trailing-edge serrations, the mechanism by which noise is reduced is likely to be quite different. Jet noise originates primarily from free-space fluctuations downstream of the nozzle exit, hence nozzle chevrons reduce noise by modifying the structure of the turbulent jet. Conversely, trailing-edge noise is dominated by the interaction of pressure fluctuations with the trailing edge itself, and changes to the flow downstream of the trailing edge will most likely have minimal impact on the trailing-edge noise, although it will be an important factor if the wake interacts with surfaces located downstream.

Understanding the mechanism by which trailing-edge serrations reduce aerofoil self-noise is therefore of clear importance. If the mechanisms were understood it could potentially lead to improvements in serration design, and possibly the development of alternative techniques based on similar physical principles. The ultimate goal of this study is therefore to perform a numerical investigation of the flow around an aerofoil with a trailing-edge modification, for the purpose of identifying the mechanisms by which the noise reduction effect is caused. In order to perform such a fundamental physical study, direct numerical simulation (DNS) is a preferred tool due to the absence of turbulence modelling. The complex geometries associated with trailing-edge modifications represent a considerable numerical challenge using high-order accuracy spatial schemes, however. For this reason a hybrid grid approach, using a body-fitted computational grid to represent an aerofoil geometry, in conjunction with a purposely developed immersed boundary (IB) representing the trailing-edge modification, is employed.

2. Simulation geometry

Aerofoil simulations have been conducted previously at $Re = 5 \times 10^4$, $M = 0.4$ for a NACA-0012 aerofoil at 5° and 7° incidence (Jones 2007; Jones, Sandberg & Sandham 2008), and more recently for a NACA-0006 aerofoil at 7° incidence (Jones, Sandham & Sandberg 2010*b*). The simulations at 7° incidence exhibit transition further upstream than the case at $\alpha = 5°$ and thicker turbulent boundary layers at the trailing edge. For the case at $\alpha = 5°$ a slightly thinner turbulent boundary layer is present, and greater tendency toward tonal behaviour at low frequencies is observed. For these reasons the case of a NACA-0012 aerofoil at $\alpha = 5°$ has been selected for the current study. The thinner boundary layer means that the trailing-edge serrations do not have to be unduly large. The presence of tonal noise at low frequency means that the effect of trailing-edge serrations upon such behaviour may also be studied.

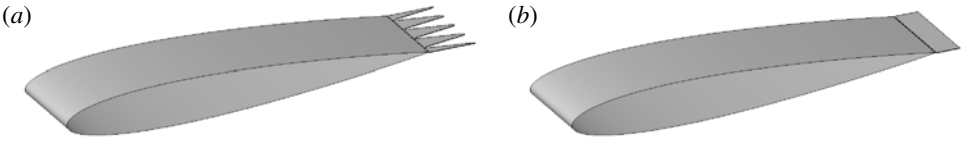

FIGURE 1. Aerofoil geometry with serrated (*a*) and straight (*b*) flat-plate trailing-edge extension.

In order to investigate the effects of trailing-edge serrations upon noise production, an appropriate serration geometry must be chosen. Although the study of Howe (1991) was conducted for the case of flow over a flat-plate aerofoil, serrations have also been observed to reduce trailing-edge noise when employed in conjunction with finite thickness aerofoils (Oerlemans *et al.* 2009; Gruber & Joseph 2011). For the current study, however, the chosen geometry is a NACA-0012 aerofoil with a serrated flat-plate extension at the trailing edge, as illustrated in figure 1(*a*). The advantage of a flat-plate geometry is that since the plate is comparatively thin, bluntness effects will be minimized, hence the presence of the serrations will cause less modification to the boundary layer and a more direct comparison between the serrated and non-serrated trailing-edge cases will be possible. Comparatively little experimental data are currently available regarding the use of trailing-edge serrations for noise reduction, and certainly not for the Reynolds number regime currently calculable by DNS. Significant noise reduction has been observed experimentally at moderate Reynolds numbers, however, for serration dimensions similar to those considered by Howe (for example Gruber & Joseph 2011). Therefore the analysis of Howe (1991) is used here as a reference in selecting an appropriate geometry. Howe describes the geometry of sawtooth trailing-edge serrations with two parameters, the spanwise wavelength λ and the streamwise root-to-tip distance $2h$, and predicts that the intensity of radiation will be reduced for frequencies satisfying $\omega h/U > 1$. Effectively, Howe states that the serrations must be of similar order size to the turbulent boundary layer. Furthermore, Howe determined that the sides of the serrations should be inclined at angles less than 45° to the free stream, i.e. $2h > \lambda$.

Our previous aerofoil simulation at $\alpha = 5°$, $Re = 5 \times 10^4$ and $M = 0.4$ yielded a displacement thickness of $\delta^*/c = 2.8 \times 10^{-2}$ at the aerofoil trailing edge. By considering this, in conjunction with Howe's relationship $\omega h/U > 1$, a serration geometry can be chosen. Dimensions of $\lambda/c = 0.05$ and $h/c = 0.06$ are selected, giving a total serration length of $2h/c = 0.12$, predicted to result in noise reduction for Strouhal numbers $St > 2.65$. The serration angle will be less than 45° as required, and a spanwise domain width of 0.2 aerofoil-chords, as employed for previous DNS, will mean that the flow over a reasonable number of serrations can be computed. To ascertain the impact of serrations upon trailing-edge noise production, it is necessary to perform an equivalent straight trailing-edge reference simulation to the serrated trailing-edge geometry, as illustrated in figure 1(*b*). The straight trailing-edge plate is specified as extending half the length of the serrated trailing edge, in order to maintain the same aerofoil surface area.

3. Direct numerical simulations

3.1. *Governing equations*

The flow under consideration is governed by the full compressible Navier–Stokes equations. The fluid is assumed to be an ideal gas with constant specific heat

coefficients. All quantities are made dimensionless using the flow quantities in the free stream, and the aerofoil chord was chosen as the reference length. The non-dimensional continuity, momentum and the energy equations are:

$$\frac{\partial \rho}{\partial t} + \frac{\partial}{\partial x_k}(\rho u_k) = 0, \tag{3.1}$$

$$\frac{\partial}{\partial t}(\rho u_i) + \frac{\partial}{\partial x_k}[\rho u_i u_k + p\delta_{ik} - \tau_{ik}] = 0, \tag{3.2}$$

$$\frac{\partial}{\partial t}(\rho E) + \frac{\partial}{\partial x_k}\left[\rho u_k\left(E + \frac{p}{\rho}\right) + q_k - u_i\tau_{ik}\right] = 0, \tag{3.3}$$

where the total energy is defined as $E = T/[\gamma(\gamma - 1)M^2] + 0.5u_i u_i$. The stress tensor and the heat–flux vector are computed as

$$\tau_{ik} = \frac{\mu}{Re}\left(\frac{\partial u_i}{\partial x_k} + \frac{\partial u_k}{\partial x_i} - \frac{2}{3}\frac{\partial u_j}{\partial x_j}\delta_{ik}\right), \quad q_k = \frac{-\mu}{(\gamma - 1)M^2 PrRe}\frac{\partial T}{\partial x_k}, \tag{3.4}$$

respectively, where the Prandtl number is assumed to be constant at $Pr = 0.72$, and $\gamma = 1.4$. The molecular viscosity μ is computed using Sutherland's law (White 1991), setting the ratio of the Sutherland constant over free-stream temperature to 0.36867. To close the system of equations, the pressure is obtained from the non-dimensional equation of state $p = (\rho T)/(\gamma M^2)$. The dimensionless form of the governing equations means that the frequency f is equivalent to a Strouhal number based on aerofoil chord, i.e. $St = f^* c/u_\infty$, where f^* is the dimensional frequency, c the aerofoil chord and u_∞ the free-stream velocity.

3.2. *Numerical method*

The compressible Navier–Stokes equations are solved using a high-order accurate numerical scheme applicable to general geometries. The extension to curvilinear coordinates is achieved through metric terms pre-multiplying the derivatives of the governing equations. No upwinding, artificial dissipation or explicit filtering are employed. Stability is rather achieved through appropriate conditioning of the governing equations, such as an entropy-splitting approach for the nonlinear terms in conjunction with a Laplacian formulation of the viscous and heat conduction terms (Sandham, Li & Yee 2002). The latter is used to avoid odd–even decoupling when using central finite-difference schemes. In addition, compatible fourth-order spatial difference operators for the interior and boundary points (Carpenter, Nordström & Gottlieb 1999) are employed. At the aerofoil surface a constant temperature ($T = 1$), no-slip condition is applied, and a periodic boundary condition is applied in the z direction. Further details on the fundamental numerical approach are given in Jones *et al.* (2008). At the inflow/free-stream boundary, characteristic boundary conditions are used in combination with traditional sponge zones. A non-reflecting zonal boundary condition is used to avoid spurious pressure-oscillations from the outflow boundary (Sandberg & Sandham 2006), which is subject to the passage of nonlinear disturbances, i.e. vortical structures. The topology of the computational domain is illustrated in figure 2. The domain possesses wake length $W = 5$ aerofoil chords and radius $R = 7.3$ aerofoil chords. The Cartesian axes are orientated such that x is aligned with the free-stream flow, y is the direction of lift, and z is the spanwise coordinate. The structure and resolution of the grid is the same as that of Jones *et al.* (2008) employing 1.7×10^8 grid-points, which was previously found to be well resolved.

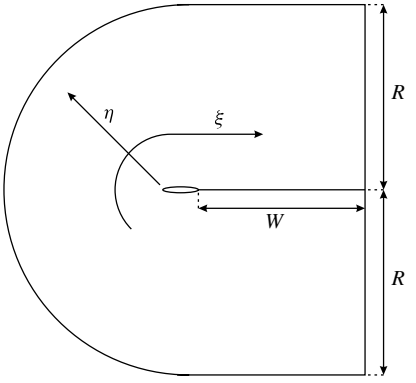

FIGURE 2. Topology of the computational domain.

Δx^+	Δz^+	Δy^+	$N_\eta : y^+ < 10$
3.36	6.49	1.0	9

TABLE 1. Grid resolution in wall units at the maximum $\overline{c}_f$ location, reproduced from Jones *et al.* (2008).

Resolution in terms of wall-units at the location of maximum skin-friction is given in table 1.

3.3. *Immersed boundary scheme*

Immersed boundary methods are used to enforce boundary conditions upon boundaries that do not coincide with computational grid points. Typically some reduction in accuracy, either in geometric representation of the boundary, or of the discretization, occurs. However, advantages of such methods are that complex geometries may be simulated without requiring complex grid generation or treatment of metric discontinuities. For a review of immersed boundary methods, see Mittal & Iaccarino (2005). The approach employed in the current study is effectively a discrete forcing approach with direct boundary imposition. A full explanation of the method is included in Sandberg & Jones (2011), where the immersed boundary method is validated for the case of flow around a cylinder and for hydrodynamic instability growth on a flat plate. In the former case a cylinder body was represented on a Cartesian grid using the immersed boundary method, and the resultant Strouhal numbers for the vortex shedding matched experimental and numerical reference data. In the latter case the immersed boundary method was employed to represent a flat plate for the simulation of a laminar boundary layer. Hydrodynamic instabilities were then introduced within the boundary layer by the addition of volume forcing, and growth rates were found to closely match those obtained using a body-fitted grid, as well as numerical reference data.

For the current study the immersed boundary method is used to represent the flat-plate extensions to the aerofoil trailing edge illustrated in figure 1. It should be noted that the grid-resolution is specified to yield $y^+ = 1$ at the wall, and ten grid-points below $y^+ = 10$, at the worst-case location of maximum skin friction for the equivalent

case without splitter plate (approximately $x = 0.7$: Jones *et al.* 2008). At the trailing edge the skin friction is less than half of this value (Jones *et al.* 2008), hence the flow is well resolved here. The flat plates are intended to be thin, but the immersed boundary method requires that the plates be at least two points thick in order to operate correctly. Since for the C-type domain grid-points are duplicated on the wake dividing line, this means that the flat-plate extensions must be three grid-points thick. This results in a flat plate 1.2×10^{-3} aerofoil chords thick. In contrast to the sharp geometries investigated by Howe (1991), for the current study both the root and tip of the trailing-edge serrations possess a finite radius of 3.5×10^{-3}.

4. Initial condition

In order to provide an initial condition for the three-dimensional simulations, the code is first run in two dimensions. The same grid is used as for the three-dimensional simulations, and a two-dimensional flat plate is added to the trailing edge with the same dimensions as that of the three-dimensional simulations. The simulation is progressed for 28 non-dimensional time units, at which point the simulation appears to have reached a statistically stationary state. At this point the simulation exhibits quasi-periodic vortex shedding from a laminar separation bubble at $St \approx 4$ (figure 3*a*). The flow field at $t = 28$ is then extruded in the z direction and used as the initial flow field for the three-dimensional simulations. For the serrated trailing-edge simulation the regions between serrations, where fluid properties cannot be specified from the two-dimensional simulation, are specified as possessing $\rho = 1$, $u_i = 0$ and $E_t = 1/(\gamma(\gamma - 1)M^2)$. At $t_{3D} = 0$ both three-dimensional simulations are subject to a perturbation in ρu_i of order 1×10^{-3}, located within the boundary layer at $x = 0.2$. The perturbation extends over a region of 3×3 grid points in the ξ and η directions, and possesses a random amplitude distribution in the z direction. The intention is to excite absolute instability mechanisms within the separation that will lead to 'self-sustaining' turbulence (Jones *et al.* 2008). No further disturbances are added, and the simulations are progressed in time. For both simulations transition occurs after approximately two time units, and the large-scale vortex shedding observed in the two-dimensional simulation ceases (figure 3*b*). Simulations are run for 23.1 time units, with time step $\Delta t = 1.4 \times 10^{-4}$, and statistical data are computed for the final 11.9 time units, corresponding to approximately 48 cycles of the low-frequency vortex shedding observed in two dimensions. Frequency domain analysis is performed employing three segments, overlapping by 50 %, and Hanning windowing. The sampling interval for statistical and frequency domain analysis is ten iterations.

5. Results

5.1. *General features of the flow*

The spanwise vorticity component for the $z = 0.1$ plane of the straight trailing-edge case is plotted in figure 3(*b*), noting that both cases appear qualitatively the same. For both three-dimensional simulations the laminar boundary layer separates near the suction-side leading edge, and reattaches as a turbulent boundary layer in the vicinity of $x = 0.5$. The developing turbulent boundary layer then convects over the trailing-edge extension. In contrast, the lower-surface boundary layer remains laminar for the extent of the aerofoil chord. The structure of the three-dimensional flow field is shown for both cases in figure 4. Iso-surfaces of the second invariant of the velocity gradient

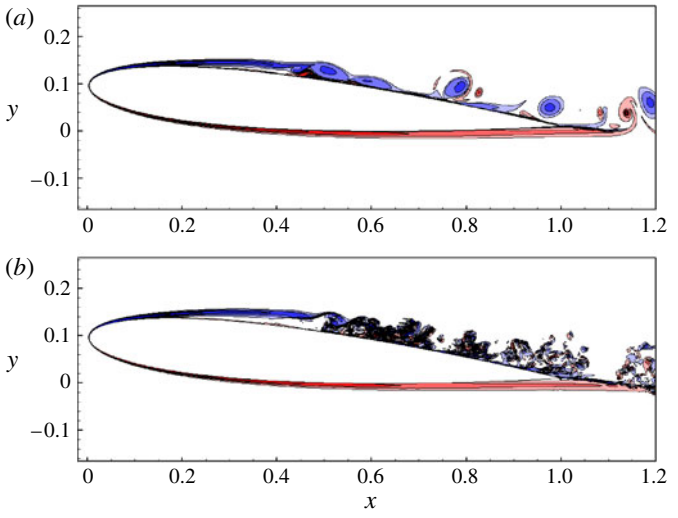

FIGURE 3. (Colour online) Iso-contours of the spanwise vorticity component for (*a*) the precursory two-dimensional simulation, and (*b*) the three-dimensional straight trailing-edge simulation, using 12 levels over the range $\omega_z = \pm 200$.

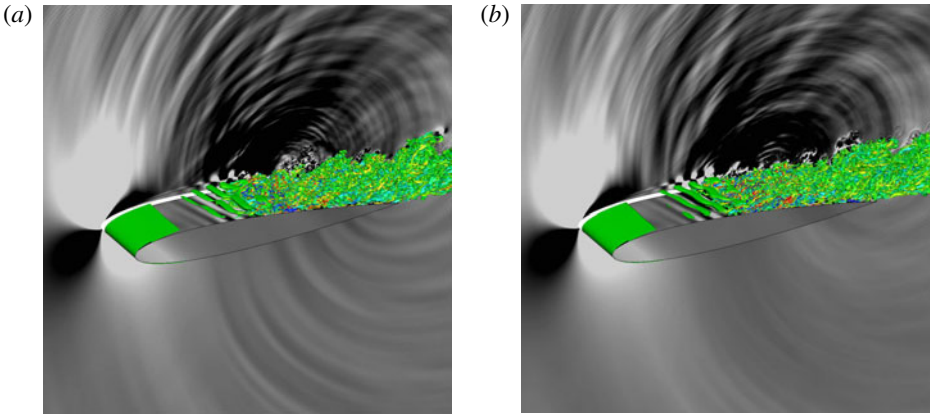

FIGURE 4. (Colour online) Iso-contours of $Q = 100$ coloured by streamwise vorticity over the range $\omega_x = \pm 100$, with background showing dilatation rate over the range $\boldsymbol{\nabla} \cdot \boldsymbol{U} = \pm 7.5 \times 10^{-2}$, for the straight (*a*) and serrated (*b*) trailing-edge cases.

tensor, defined by

$$Q = \tfrac{1}{4}(\Omega_i \Omega_i - 2 S_{ij} S_{ij}), \tag{5.1}$$

where S_{ij} is the shear stress and Ω_{ij} the strain rate, illustrate the presence of hydrodynamic instabilities within the laminar region of the suction-side boundary layer. At the aerofoil mid-chord, large structures, appearing 'roller'-like in the straight trailing-edge case, are observed to rapidly break down to small scales, and a turbulent boundary layer results.

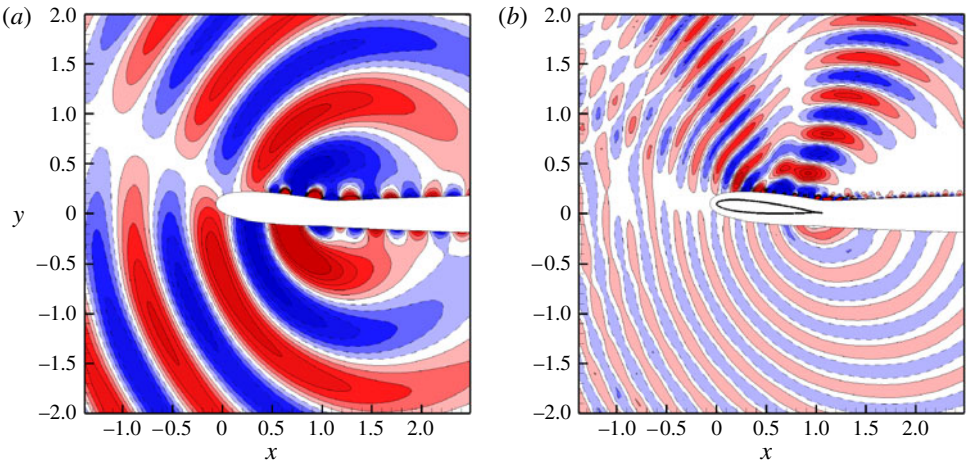

FIGURE 5. (Colour online) The real part of acoustic pressure computed at the aerofoil mid-span for the straight trailing-edge case, at Strouhal numbers $St = 2.05$ (*a*) and $St = 6.50$ (*b*). Negative contours are represented by dashed lines.

5.2. *The effect of serrations upon acoustic behaviour*

The effect of trailing-edge serrations upon the acoustic behaviour will be investigated first before analysing the hydrodynamic behaviour of the flow. Acoustic waves are illustrated by plotting iso-contours of ∇u_i. All simulations exhibit larger-amplitude acoustic waves above the aerofoil. This is because the transition/reattachment region is an important noise source for the current configuration (Jones *et al.* 2010*b*), which dominates over trailing-edge noise at high frequencies. The acoustic radiation above the aerofoil can therefore be considered to be the sum of the trailing-edge noise and the additional noise sources on the upper aerofoil surface, whilst the acoustic radiation below the aerofoil consists solely of trailing-edge noise. The acoustic waves below the aerofoil are therefore weaker in intensity and originate from the trailing edge. Whereas it is difficult to detect any difference between the two cases for the acoustic field above the aerofoil, acoustic waves below the aerofoil appear to be slightly weaker for serrated trailing-edge cases than for the equivalent straight trailing-edge cases, implying that the trailing-edge noise contribution of the aerofoil self-noise is affected by the serrations.

Plotting the real part of pressure for a comparatively low Strouhal number $St = 2.05$ and a higher Strouhal number $St = 6.5$ is representative of the two noise sources present for the flow (figure 5). At low frequencies trailing-edge noise is dominant, resulting in a noise radiation pattern symmetric about the aerofoil chord line. At higher frequencies the additional noise sources on the upper aerofoil surface become more important, resulting in an asymmetric radiation pattern with additional lobes originating from the upper aerofoil surface. An overview of differences between the cases is provided by plotting pressure power spectra in the free stream at $(x, y) = (0.5, \pm 1.0)$, both above and below the aerofoil (figure 6). When considering acoustic radiation above the aerofoil it is difficult to determine any difference between serrated and straight trailing-edge cases. This is because the radiation above the aerofoil includes noise generated by the additional sources located on the upper aerofoil surface, which will not be affected by modifications to the trailing edge.

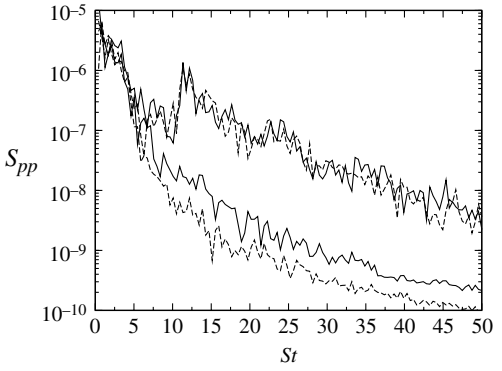

FIGURE 6. Pressure power spectra for the straight (—) and serrated (- - -) trailing-edge cases. The greater amplitude signal is recorded above the aerofoil at $(x, y) = (0.5, 1.0)$, and the lesser amplitude signal below the aerofoil at $(x, y) = (0.5, -1.0)$.

However, the sound radiation recorded below the aerofoil exhibits clear differences between serrated and straight trailing-edge cases. The acoustic power is reduced significantly over a wide range of Strouhal numbers, most significantly for $St > 5$, and this noise reduction behaves similarly to Howe's analytic result, in that the noise reduction occurs for all Strouhal numbers greater than $St \approx 5$. This contrasts with experiments by Oerlemans *et al.* (2009) and Gruber & Joseph (2011), where a noise increase was observed above a certain onset frequency. The noise reduction observed here varies in the range 6–10 dB, contrasting with experimentally observed average noise reductions up to approximately 3 dB, or up to 10 dB for narrow frequency bands (Oerlemans *et al.* 2009), and hence is significant in magnitude.

Before analysing the acoustic pressure further, it is useful to consider ways in which the presence of trailing-edge serrations may potentially affect the trailing-edge noise-production mechanism. Trailing-edge noise propagates in a predominantly upstream direction, symmetric about the trailing edge. For a straight trailing edge subject to the passage of a spanwise homogeneous turbulent boundary layer, the radiated noise will also be spanwise homogeneous, and the acoustic power will decay proportional to $1/r^2$, where r is the perpendicular distance from the aerofoil trailing edge. For a serrated geometry, each serration possesses two edges, inclined at an angle $\pm\theta$ with respect to the z-axis. For the geometry investigated here this is approximately $\pm 85.5°$. Clearly it could be hypothesized that by locally inclining the trailing edge to the z-axis in an alternating positive/negative fashion, the directivity and spanwise correlation of the trailing-edge noise may be altered. For example, where spanwise coherent (typically low-frequency) disturbances convect over a trailing edge they generate similarly coherent trailing-edge noise (Sandberg, Jones & Sandham 2008). It is feasible that if a spanwise coherent disturbance were to convect over a serrated trailing edge, the scattered pressure might exhibit decreased spanwise correlation. Furthermore, the inclination of local trailing-edge elements to the z-axis could feasibly lead to a change in directivity. For example, the acoustic pressure may be radiated with an 'out-of-plane' (i.e. z-velocity) directivity, leading to decreased upstream power ($\theta = -120°$) but not modifying radiation in the vertical direction ($\theta = \pm 90°$).

In order to provide insight into these hypotheses, and having determined Strouhal numbers where trailing-edge noise reduction occurs, the directivity of the aerofoil self-noise will be investigated for finite Strouhal number bands, selected based on the physics of the flow, as follows.

$2 < St < 5$. This Strouhal number range lies below that where pronounced noise reduction due to the presence of trailing-edge serrations is expected. Any tonal behaviour associated with quasi-two-dimensional vortex shedding is expected to lie within this range, and aerofoil self-noise is expected to be dominated by trailing-edge noise both above and below the aerofoil. The lower threshold of $St = 2$ removes very low-frequency noise produced by non-vortical events (e.g. undulations in the potential flow).

$5 < St < 10$. In this interval noise reduction is expected for the case with trailing-edge serrations. This frequency range is expected to contain the most convectively amplified hydrodynamic instability waves ($St \approx 8.5$ for an equivalent case without splitter plate: Jones, Sandberg & Sandham 2010*a*), and aerofoil self-noise is expected to be dominated mostly by trailing-edge noise at the lower frequencies and the additional (suction surface) noise sources at high frequencies.

$10 < St < 15$. In this interval noise reduction is expected for the case with trailing-edge serrations. Above the aerofoil the self-noise is expected to be dominated by the additional noise sources, whilst below the aerofoil only trailing-edge noise will be present.

$20 < St < 25$. In this high-frequency range noise reduction is again expected for the splitter plate with trailing-edge serrations. Above the aerofoil the self-noise is expected to be dominated by the additional noise sources, whilst below the aerofoil only trailing-edge noise will be present.

The acoustic power directivity is plotted in figure 7. Considering first the interval $2 < St < 5$, it can be seen that the aerofoil self-noise is approximately symmetric about the aerofoil chord for both cases. Variations exist between the serrated and straight trailing-edge cases predominantly above the aerofoil. It is not clear why this is the case since the self-noise in this interval is expected to be dominated by trailing-edge noise, which radiates symmetrically, and any change in the trailing-edge noise amplitude would be expected to manifest as a symmetric change also. It is interesting to note that even at this low frequency the serrations appear to yield a considerable noise reduction for all angles of propagation. For $5 < St < 10$ the influence of the additional noise sources becomes apparent; the acoustic radiation above the aerofoil exhibits greater amplitude than that below the aerofoil for both cases, with a pronounced upstream orientated lobe that is not present below the aerofoil. A significant reduction in trailing-edge noise is observed for the serrated case (below the aerofoil). This reduction in trailing-edge noise is presumably at least partly responsible for the reduction in radiation amplitude observed above the aerofoil. In the range $10 < St < 15$ the additional noise sources are dominant, and we see that whilst the radiation below the aerofoil is reduced for the serrated cases the radiation above the aerofoil is not. Similar behaviour occurs for $20 < St < 25$, but the amount by which the trailing-edge noise decreases is reduced. For both $10 < St < 15$ and $20 < St < 25$ there is significant radiation downstream of the aerofoil at $-60 < \theta < -10$. This noise does not appear reduced by the serrations, and its origin is not clear. At very high frequencies aerofoil self-noise can be observed to propagate downstream with low amplitude (Jones, Sandberg & Sandham 2009). However, it is also feasible that radiation from quadrupole sources in the turbulent wake are significant in amplitude in this frequency range.

In terms of general trends, it is apparent that the principal direction to which the trailing-edge noise radiates is approximately $\pm 120°$. Where the trailing-edge noise is reduced in amplitude by the presence of the serrations, it always reduces most strongly in this principal direction. For the directivity of trailing-edge noise to be consistent

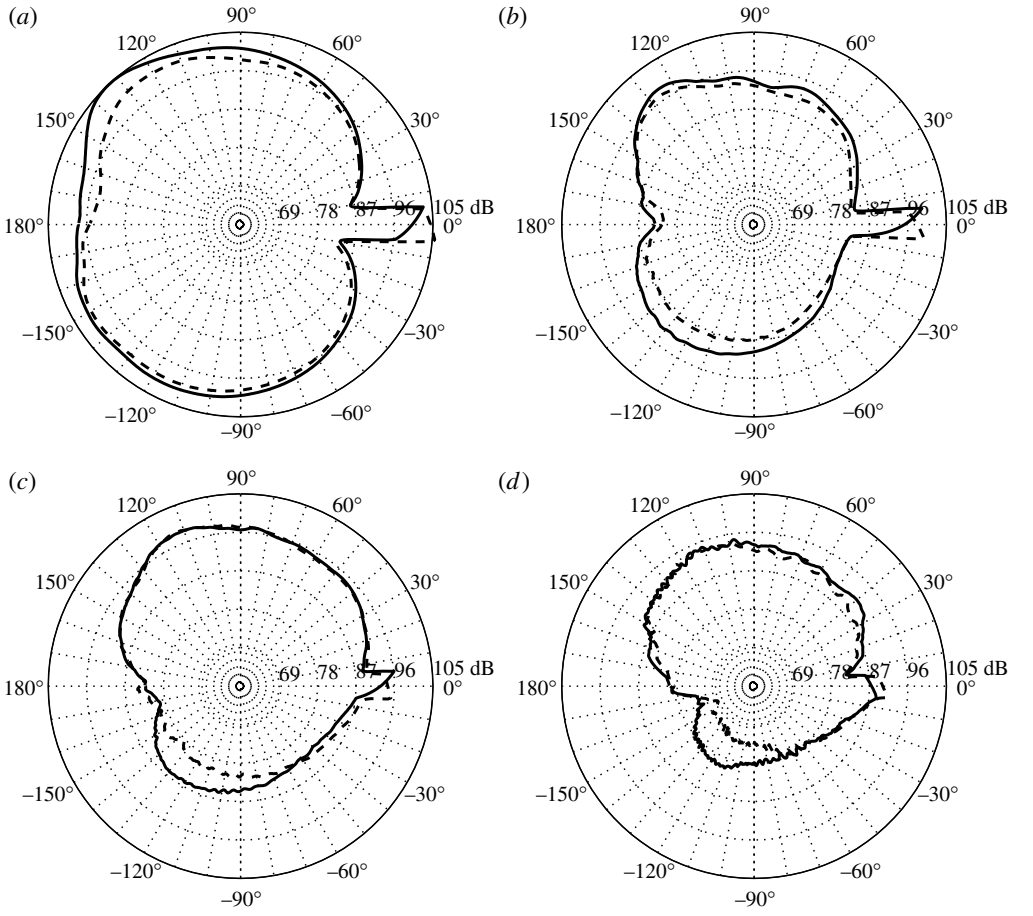

FIGURE 7. Acoustic power directivity, computed at radius $r = 2$ about the aerofoil trailing edge for finite Strouhal number intervals, showing the straight (—) and serrated (- - -) trailing-edge cases: (*a*) $2 < St < 5$; (*b*) $5 < St < 10$; (*c*) $10 < St < 15$; (*d*) $20 < St < 25$.

with the theory of 'out-of-plane' radiation, one would expect the acoustic power to decrease more significantly in the upstream direction than in the directions normal to the splitter plate surface, but this does not appear to be the case. In summary it appears that for the Strouhal number intervals where (i) the amplitude of the original trailing-edge noise is significant, and (ii) the amount of the noise reduction is most significant, the presence of the trailing-edge serrations acts to reduce the trailing-edge noise without significantly modifying its directivity. Hence based on these results there is no compelling evidence for 'out-of-plane' radiation behaviour.

Spanwise correlations of surface pressure are computed as

$$C_{zz}(\Delta z, f) = \left\langle \frac{p(z,f)\overline{p}(z+\Delta z,f)}{p\,(z,f)^2} \right\rangle \tag{5.2}$$

for the same Strouhal number intervals as before, and plotted in figure 8. Since the lower aerofoil surface is subject to a favourable pressure gradient, the only pressure fluctuations present here consist of acoustic waves originating at the aerofoil trailing

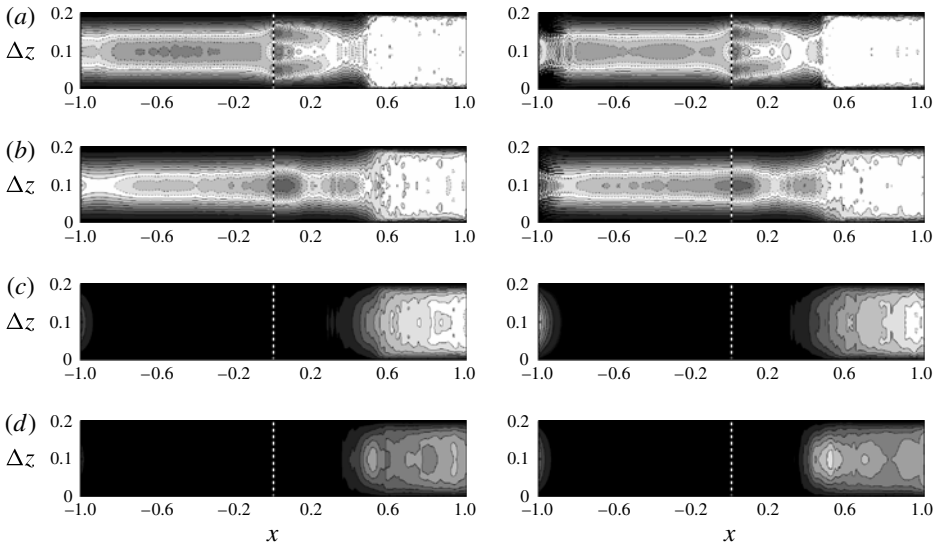

FIGURE 8. Iso-contours of spanwise correlation coefficient $C_{zz} = \pm 0.95$ using 16 levels, showing the straight (left) and serrated (right) trailing-edge cases. Negative contours are plotted with dashed lines. The upper aerofoil surface is represented by positive values of x and the lower aerofoil surface is represented by negative values of x: (*a*) $20 < St < 25$; (*b*) $10 < St < 15$; (*c*) $5 < St < 10$; (*d*) $2 < St < 5$.

edge, and the spanwise coherence of the acoustic pressure can be observed here. It can be seen that for Strouhal number intervals $2 < St < 5$ and $5 < St < 10$ the acoustic pressure is strongly correlated in the spanwise direction, whereas for $10 < St < 15$ and $20 < St < 25$ it exhibits much weaker correlation. The spanwise correlations appear similar for both serrated and straight trailing-edge cases. Thus on the basis of this evidence it does not appear that the presence of a serrated trailing edge significantly alters the spanwise correlation of the acoustic pressure for the current case.

5.3. *Hydrodynamic input to the trailing-edge noise mechanism*

Significant trailing-edge noise amplitude reductions have been observed for the Strouhal number range $5 < St < 20$, for the serrated trailing-edge case. Before analysing the flow around the serrations themselves, it is pertinent to analyse the turbulent boundary layer that convects over the trailing edge for each case. The turbulent boundary layer is effectively the 'input' to the trailing-edge noise production mechanism (e.g. in the theory of Amiet 1976), and any differences in behaviour here that could cause differences in the trailing-edge noise must be quantified before proceeding further. Time-averaged boundary layer profiles are plotted at $x = 0.99$ for both cases in figure 9. It can be seen that the boundary layer profiles for both cases are similar, and that the profiles do not closely match either the inner or log law behaviours. This is perhaps unsurprising because of the low Reynolds number of the flow, in conjunction with the presence of an adverse pressure gradient in this region. Profiles recorded further upstream ($x = 0.9$) more closely match the viscous sublayer. Reynolds stress components at $x = 0.99$ are plotted in figure 10 and appear in general qualitatively similar for both cases, with $\overline{v'v'}$ and $\overline{w'w'}$ exhibiting a single maximum at approximately the same location within the boundary layer. The quantity $\overline{u'u'}$

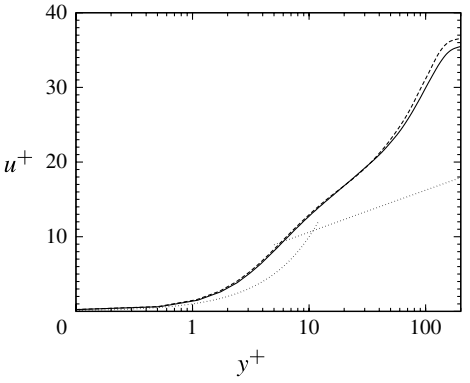

FIGURE 9. Turbulent boundary layer profile at $x = 0.99$ for the straight (−) and serrated (- -) trailing-edge cases. The fine dashed lines illustrate $u^+ = y^+$ and $u^+ = 1/0.41\log(y^+) + 5$.

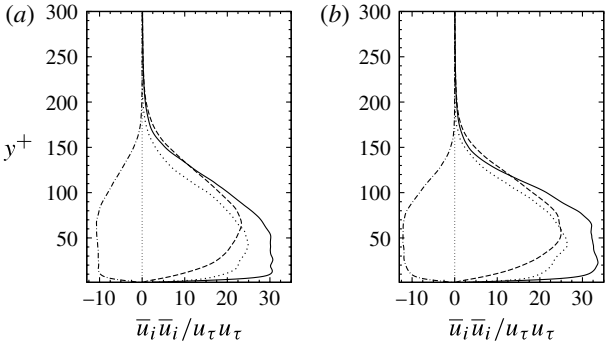

FIGURE 10. Reynolds stress components at $x = 0.99$ for the straight (*a*) and serrated (*b*) trailing-edge cases, showing $\overline{u'u'}$ (—), $\overline{v'v'}$ (- - -), $\overline{w'w'}$ (· · ·), and $\overline{u'v'}$ (−·).

exhibits a maximum near the aerofoil surface for both cases. The amplitude of the Reynolds stress components does not appear to be lower for the serrated trailing-edge case, however, and in fact appears to be slightly greater overall. Turbulent spectra within the boundary layer at $x = 1.0$ are plotted for both cases in figure 11. In this instance the spectra were computed with a three-point running average in order to remove small-scale fluctuations that make comparisons difficult, particularly for higher frequencies. The turbulent spectra at this point are very similar between serrated and straight trailing-edge cases. Finally, if we refer back to the spanwise correlations illustrated in figure 8, we can see that the spanwise correlation of surface pressure in the turbulent boundary layer appears very similar for both the serrated and straight trailing-edge cases. For similar flow parameters Sandberg & Jones (2011) determined that the presence of (comparatively shorter) trailing-edge serrations does not affect the transition process, e.g. via an acoustic feedback process involving the trailing edge (Jones *et al.* 2010*a*). The similarity of the hydrodynamic behaviour upstream of the trailing edge between the two cases appears to confirm this result for the serration geometry investigated here.

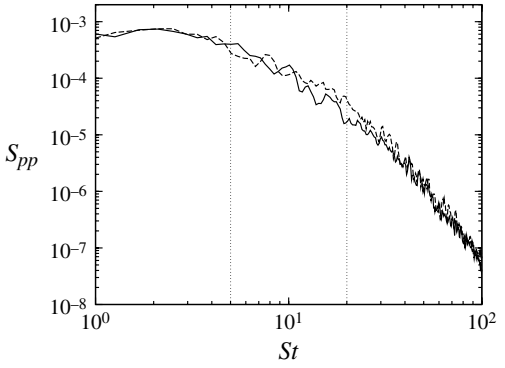

FIGURE 11. Pressure spectra computed within the turbulent boundary layer at $x = 1.0$ for the straight (—) and serrated (- - -) trailing-edge cases. Dotted lines indicate the region where the maximum trailing-edges noise reduction is observed.

5.4. *The structure of the flow around trailing-edge serrations*

In the previous section it was determined that there are no significant differences between the turbulent boundary layers for the straight and serrated trailing-edge cases that could account for the observed reductions in trailing-edge noise. This means that any significant changes in trailing-edge noise amplitude must be caused either by modification to the scattering process itself, or by other hydrodynamic behaviour local to the trailing edge. In this section the flow in the direct vicinity of the trailing-edge splitter plates will be investigated. Plotting iso-surfaces of Q in the vicinity of the trailing edge illustrates differences in the flow here (figure 12). Due to the unpredictable nature of turbulent flow, animations provide a greater insight into their behaviour than single images, and inform the analysis presented here. For both cases a wide range of turbulent spatial scales is present, including streamwise orientated, spanwise orientated and horseshoe-type vortices. When viewed for a period of time, two main differences can be ascertained between the two cases. Firstly, for the serrated trailing-edge case, the presence of the serrations appears to enforce a limit to the maximum spanwise extent of turbulent structures, at least in direct vicinity of the trailing edge; turbulent structures appear to be limited to a spanwise dimension of one serration width. This contrasts with the straight trailing-edge case, whereby quasi-two-dimensional structures can be observed to occur intermittently that extend for nearly the full domain width. Secondly, the presence of the serrations seems to promote the development of horseshoe-type vortices in the wake. Horseshoe vortices are known to occur in turbulent boundary layers, particularly at low Reynolds numbers (Head & Bandyopadhyay 1981), and as such can also be observed for the straight trailing-edge case. However, for the serrated trailing-edge case horseshoe vortices are observed to occur with more regularity, and to originate from the serrations themselves. The loops of these horseshoe vortices are observed to protrude through the gap between adjacent serrations, into the flow below the splitter plate. The horseshoe vortices grow as they convect downstream, trailing 'legs' that extend into the turbulent flow above the splitter plate. The horseshoe vortices appear most coherently in the region approximately one serration-length downstream of the serration tips (i.e. $1.12 < x < 1.24$), downstream of which they are more difficult to discern due to their deformation and mixing in the wake. For each horseshoe vortex the leg with the lesser z-coordinate shows a tendency toward negative streamwise vorticity, whilst the leg

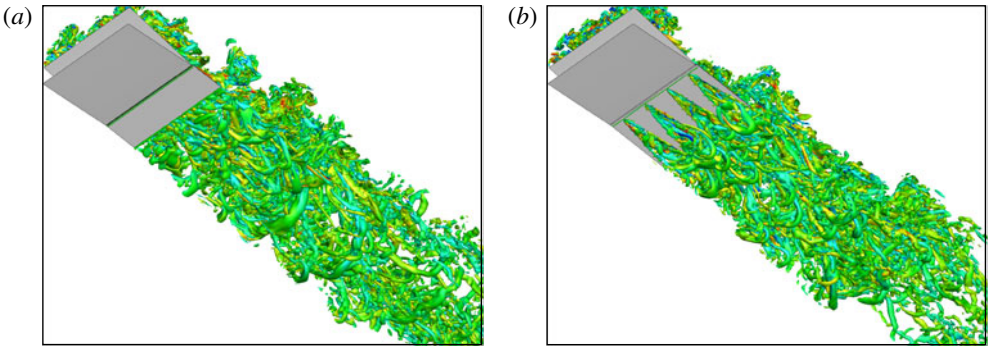

FIGURE 12. (Colour online) Iso-contours of $Q = 100$ coloured by streamwise vorticity over the range $\omega_x = \pm 100$ for the straight (a) and serrated (b) trailing-edge case.

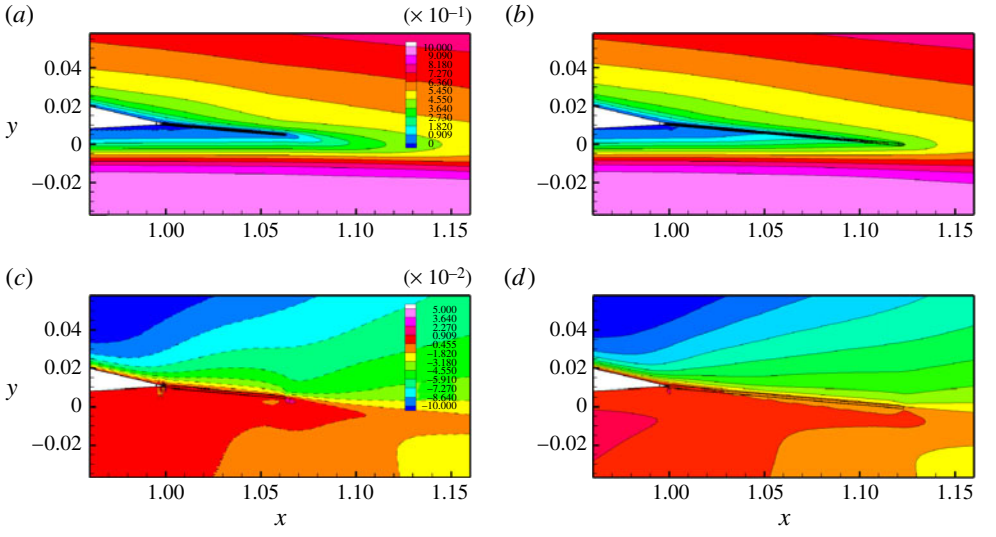

FIGURE 13. (Colour online) Iso-contours of mean velocity components for the straight (a,c) and serrated (b,d) trailing-edge cases: (a,b) $0 < \overline{u} < 1$; (c,d) $-1 \times 10^{-1} < \overline{v} < 5 \times 10^{-2}$.

with the greater z-coordinate displays a tendency toward positive streamwise vorticity. This is counter-intuitive, as it means that these structures are rotating in the opposite direction to that expected of the mean flow over the serrations.

Figure 13 illustrates the mean (spanwise averaged) velocity components. Plotting $\overline{u}$ illustrates that the serrated trailing-edge case possesses positive u-velocity in the vicinity of the trailing-edge serrations as expected. Considering both $\overline{u}$ and $\overline{v}$ it can be seen that the straight trailing edge imparts a greater discontinuity on the spanwise averaged mean flow, localized to the trailing edge itself, as opposed to the serrated trailing-edge case which exhibits a smoother streamwise evolution of properties, although a small discontinuity in $\overline{v}$ can be observed in the vicinity of the serration tips. The behaviours of the Reynolds stress components are illustrated in figures 14 and 15, showing that the amplitudes of the Reynolds stress components within the

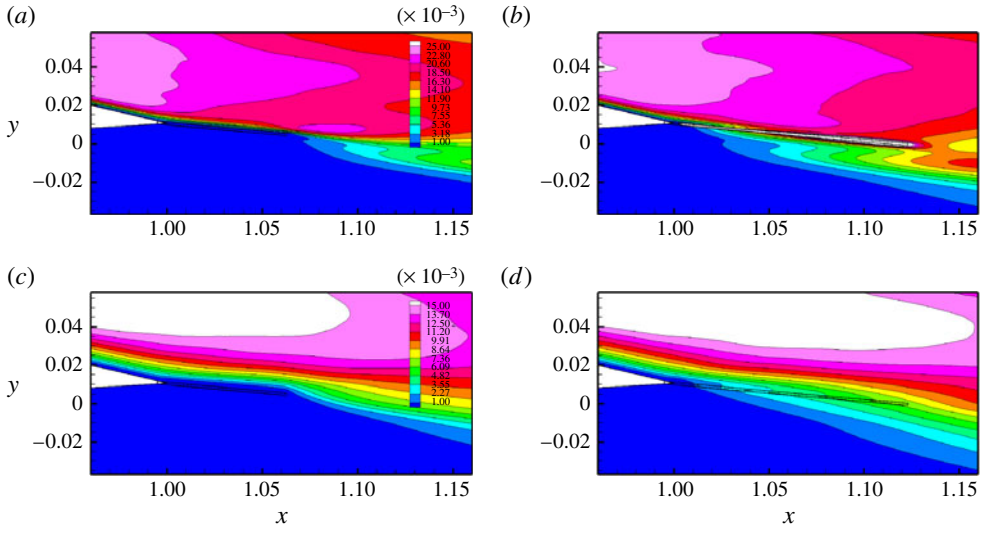

FIGURE 14. (Colour online) Iso-contours of Reynolds stresses for the straight (*a*,*c*) and serrated (*b*,*d*) trailing-edge cases: (*a*,*b*) $1 \times 10^{-3} < \overline{u'u'} < 2.5 \times 10^{-2}$; (*c*,*d*) $1 \times 10^{-3} < \overline{v'v'} < 1.5 \times 10^{-2}$.

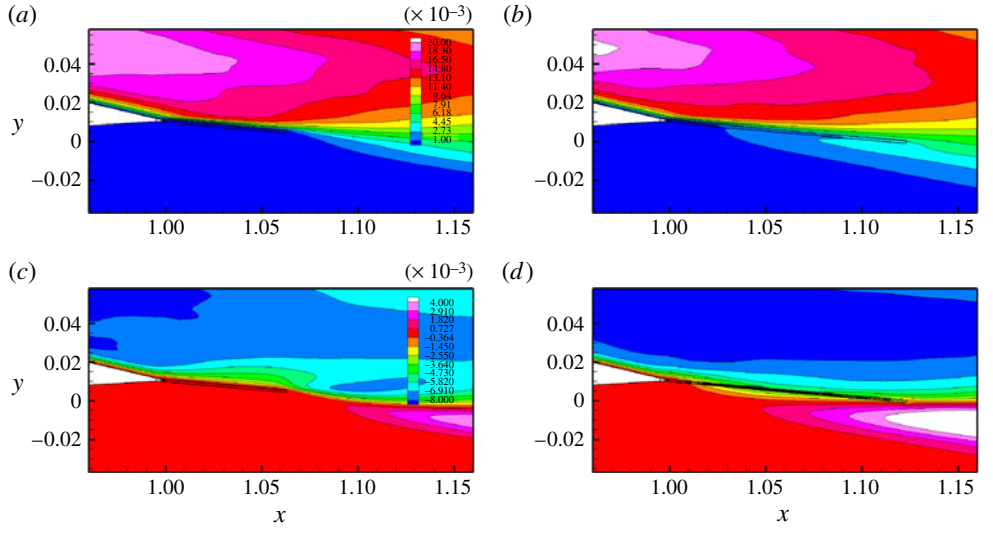

FIGURE 15. (Colour online) Iso-contours of Reynolds stresses for the straight (*a*,*c*) and serrated (*b*,*d*) trailing-edge cases: (*a*,*b*) $1 \times 10^{-3} < \overline{w'w'} < 2 \times 10^{-2}$; (*c*,*d*) $-8 \times 10^{-3} < \overline{u'v'} < 4 \times 10^{-3}$.

turbulent boundary layer are approximately the same for both cases as observed in § 5.3. The most complex behaviour is observed in $\overline{u'u'}$. For both cases $\overline{u'u'}$ exhibits a local maximum below the wake dividing line, which increases in amplitude with distance downstream from the aerofoil trailing edge, extending for a finite distance downstream of the trailing edge. Although present for both cases this behaviour is most significant for the serrated trailing-edge case; by $x = 1.16$ the amplitude of $\overline{u'u'}$

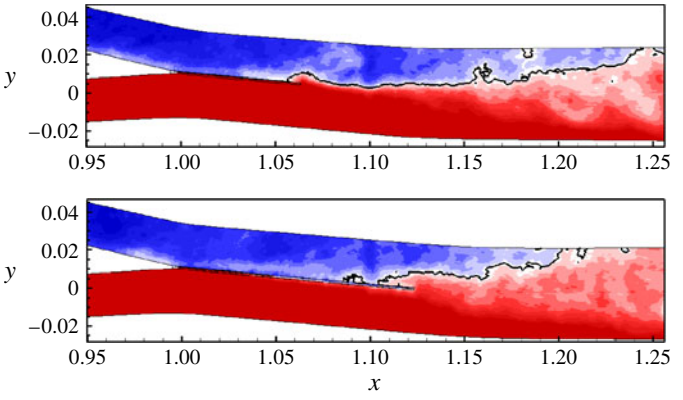

FIGURE 16. (Colour online) Iso-contours of the spanwise average of $\Gamma = \pm 0.3$, showing 16 levels. The black line illustrates $\Gamma = 0$.

below the wake centreline is of a similar order to that associated with the turbulent flow originating from the upper aerofoil surface. A second interesting behaviour occurs in $\overline{u'u'}$ for the straight trailing-edge case only. There is another local maximum in $\overline{u'u'}$, located directly downstream of the straight trailing edge and above the wake centreline. Although a near-wall peak in $\overline{u'u'}$ is not unexpected, in this instance it appears that $\overline{u'u'}$ has increased in amplitude with downstream distance from the trailing edge, contrasting with the trend for decaying $\overline{u'u'}$ away from the wall. The quantities $\overline{v'v'}$ and $\overline{w'w'}$ exhibit a simpler distribution. For the straight splitter plate, $\overline{v'v'}$ and $\overline{w'w'}$ display a smooth streamwise evolution downstream of the trailing edge, increasing in amplitude below the wake centreline due to the turbulent mixing in the wake. For the serrated trailing-edge case $\overline{v'v'}$ and $\overline{w'w'}$ appear to 'bleed' through the serrations, and again increase in amplitude below the wake centreline with increasing distance downstream of the trailing edge. In contrast to $\overline{u'u'}$, the distribution could be compared to the mixing of a passive scalar. The quantity $\overline{u'v'}$ displays maxima and minima closely related to those observed in $\overline{u'u'}$, although the sign of $\overline{u'v'}$ changes across the wake centreline due to the change in sign of $\mathrm{d}u/\mathrm{d}y$.

The spatial structure of the turbulence can be investigated by computing the variable

$$\Gamma = \frac{\langle p_x p_x \rangle - \langle p_z p_z \rangle}{\langle p_x p_x \rangle + \langle p_z p_z \rangle}, \tag{5.3}$$

where p_{x_i} refers to the partial derivative of p with respect to x_i. Where $\Gamma = 1$ streamwise gradients are dominant, hence the flow is dominated by spanwise orientated structures (or else is laminar), and where $\Gamma = -1$ indicates that spanwise gradients are dominant, hence the flow is dominated by streamwise orientated structures. The variable Γ has been computed from a set of 14 instantaneous data sets of the flow, taken over a time interval of $\Delta t = 9.8$, averaged across the aerofoil span, and is illustrated in figure 16. The first observation is that below the aerofoil, where the flow is laminar, $\Gamma = 1$ (because $p_z = 0$). Above the aerofoil, in the turbulent boundary layer, $\Gamma \approx -0.3$ and hence the flow is dominated by streamwise orientated structures (i.e. streak-like boundary-layer structures). For both cases Γ increases downstream of the trailing edge, eventually becoming positive, indicating a tendency toward a more spanwise coherent flow. Directly at the trailing edge itself there is a local maximum present for the straight splitter plate case that is not present for the

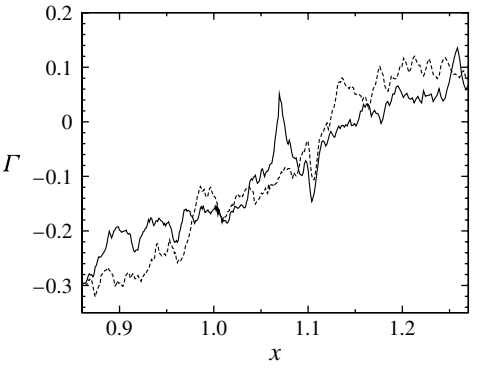

FIGURE 17. The spanwise and wall-normal average of $\Gamma = \pm 0.3$ for the upper aerofoil surface and upper wake, showing the straight (—) and serrated (- - -) trailing-edge cases.

serrated case. This is presumably related to the streamwise gradients imparted to the flow by the trailing edge itself. Despite this maximum, it appears that downstream of the trailing edge Γ increases more rapidly for the serrated case. These observations are illustrated clearly by plotting a one-dimensional variation in Γ (figure 17), formed by further averaging Γ in the wall-normal direction for all points above the wake centreline. This implies that the straight trailing edge imparts a more spanwise coherent perturbation to the turbulence in the boundary layer. The evolution of the wake towards a more spanwise-structure-dominated flow appears slightly more rapid for the serrated trailing-edge case, however, in terms of the rate of change of Γ from negative to positive with location downstream of the trailing edge.

Spanwise correlations of pressure are illustrated in figures 18–21, as computed for the same frequency intervals investigated in § 5.2. For the frequency interval $20 < St < 25$ it is not possible to detect any significant differences between cases, either as the flow convects over the aerofoil trailing edge or in the wake; the presence of the serrations does not appear to affect spanwise correlation levels over this frequency range, hence discussion will focus on the lower frequency intervals.

For the straight trailing-edge case correlation levels in the turbulent boundary layer do not vary significantly as the flow convects over the surface of the splitter plate, as expected. The effect of the trailing edge can be clearly distinguished, however, imparting a streamwise discontinuity on the correlation distribution, which is most noticeable for $2 < St < 5$. For the serrated case different behaviour occurs; unlike for the straight splitter plate, correlation levels do change as the flow convects over the surface of the serrated trailing edge. This is apparent only for frequencies $2 < St < 5$ and $5 < St < 10$, where correlation levels decrease to a minimum directly above the serrated trailing edge. It may be hypothesized that this decrease in spanwise correlation levels over the serrations corresponds to the deformation of turbulent structures. The fact that this is only apparent for the lower frequency ranges would be consistent with this hypothesis, since turbulent structures associated with low frequencies would also be associated with longer length scales, and hence more likely to be deformed by flow over or through the serrations. This would further be consistent with the observations discussed in § 5.4, that for the serrated trailing-edge case turbulent structures appear to be limited to a spanwise extent of the order of one serration wavelength within the aerofoil wake.

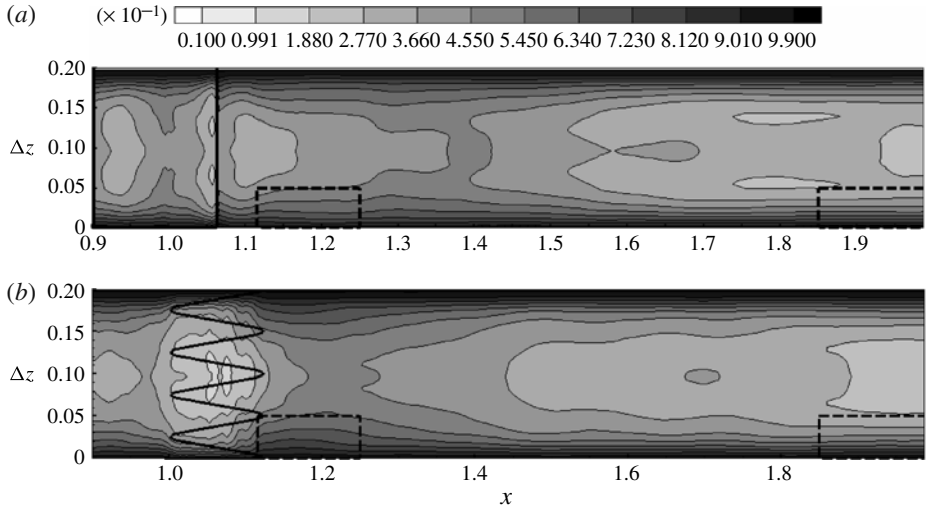

FIGURE 18. Two-point spanwise correlation of pressure for the straight (*a*) and serrated (*b*) trailing-edge cases plotted for Strouhal number $St = 3.37$, employing one-third octave averaging and showing 12 levels over the range $0.01 < C_{zz} < 0.99$. The dashed boxes highlight regions referred to in the text.

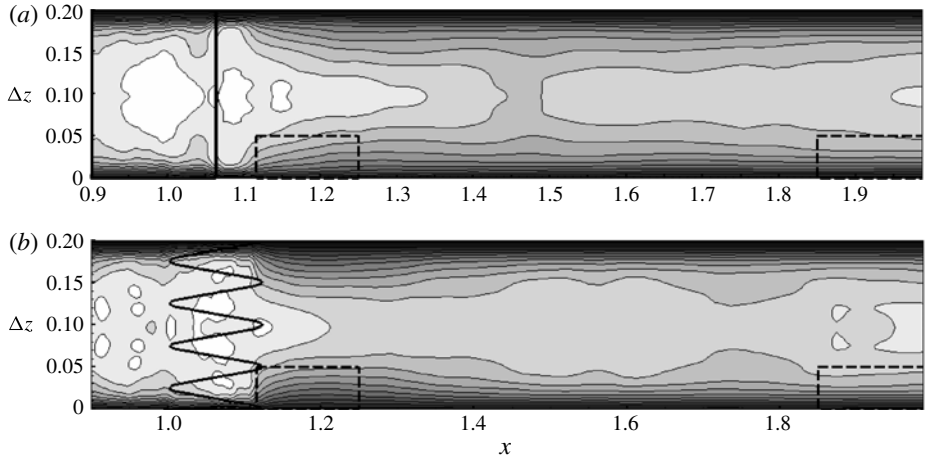

FIGURE 19. Two-point spanwise correlation of pressure for the straight (*a*) and serrated (*b*) trailing-edge cases plotted for Strouhal number $St = 7.75$, employing one-third octave averaging and showing 12 levels over the range $0.01 < C_{zz} < 0.99$.

Further differences can be observed in the region immediately downstream of the aerofoil trailing edge. For the straight trailing edge, the behaviour in this region appears to be frequency-dependent. For $2 < St < 5$, despite the streamwise discontinuity imparted by the trailing edge, correlation levels do not change significantly in the near-wake. For $5 < St < 10$ and $10 < St < 15$, however, correlation levels reduce to a minimum for a short streamwise distance directly downstream of the trailing edge, most noticeably in the range $0 < \Delta z < 0.05$, before increasing into

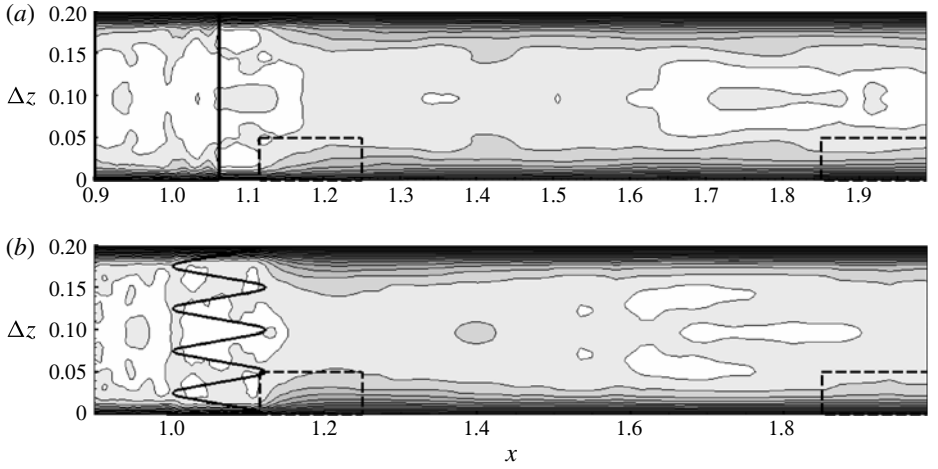

FIGURE 20. Two-point spanwise correlation of pressure for the straight (*a*) and serrated (*b*) trailing-edge cases plotted for Strouhal number $St = 11.2$, employing one-third octave averaging and showing 12 levels over the range $0.01 < C_{zz} < 0.99$.

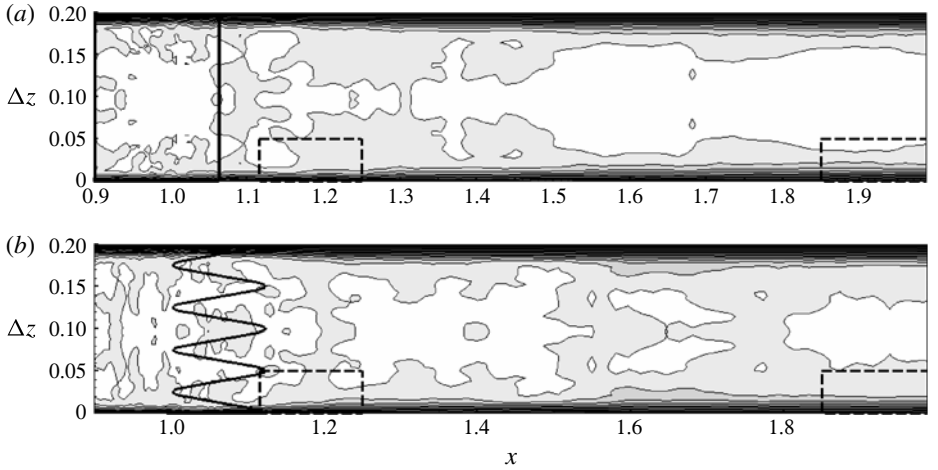

FIGURE 21. Two-point spanwise correlation of pressure for the straight (*a*) and serrated (*b*) trailing-edge cases plotted for Strouhal number $St = 15$, employing one-third octave averaging and showing 12 levels over the range $0.01 < C_{zz} < 0.99$.

the wake. Further downstream correlation levels vary more slowly. In contrast, for the serrated trailing edge the reverse happens. Directly downstream of the serration tips correlation levels increase immediately and significantly, particularly in the range $0 < \Delta z < 0.05$. Correlation levels in this region are a maximum, and decrease moving downstream into the wake. This region has been highlighted with a dashed box, and by comparison it can be seen that correlation levels in this region are in fact higher than for the straight trailing-edge case. That the presence of serrations may increase spanwise correlation levels for $0 < \Delta z < 0.05$ is perhaps a counter-intuitive result, but it is consistent with the repeated formation of horseshoe vortices between serrations,

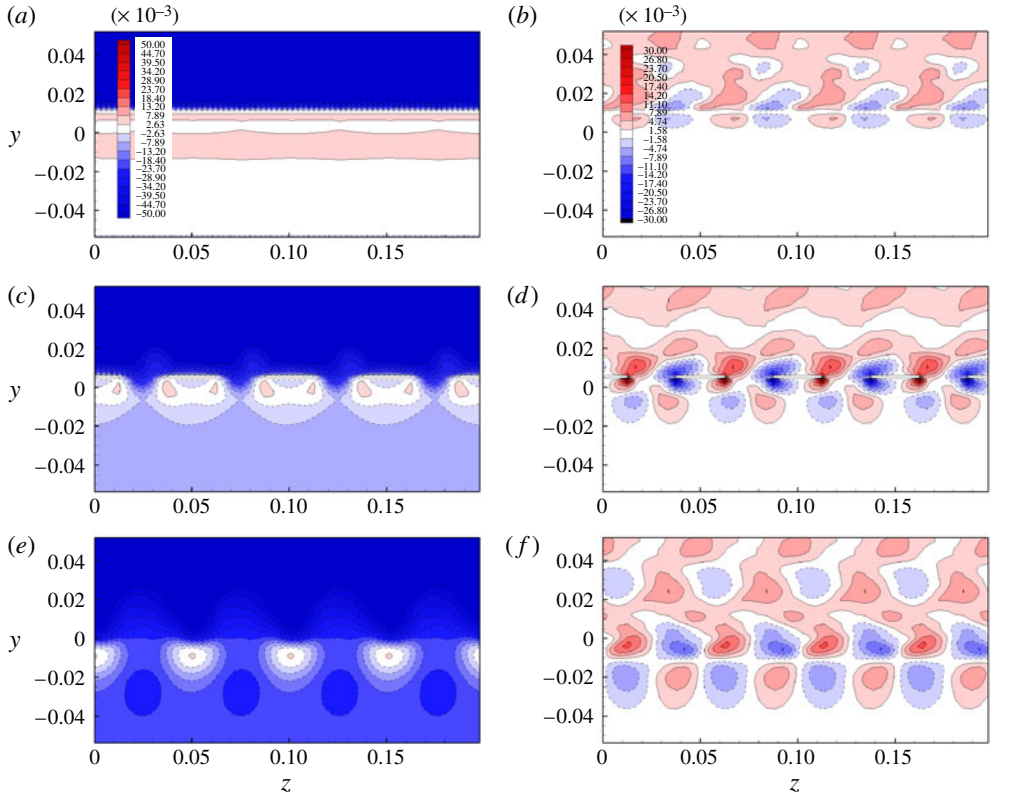

FIGURE 22. (Colour online) Iso-contours of the wall-normal velocity $v_n = \pm 4 \times 10^{-2}$ (*a*,*c*,*e*) and $\overline{w} = \pm 3 \times 10^{-2}$ (*b*,*d*,*f*) for the serrated trailing-edge case, as computed for y–z planes at x-locations indicated: (*a*) $\overline{v_n}$ at $x = 1.00$; (*b*) $\overline{w}$ at $x = 1.00$; (*c*) $\overline{v_n}$ at $x = 1.06$; (*d*) $\overline{w}$ at $x = 1.06$; (*e*) $\overline{v_n}$ at $x = 1.15$; (*f*) $\overline{w}$ at $x = 1.15$. Negative contours are represented by dashed lines.

observed in § 5.4, as it may represent 'self-correlation' between opposite legs of the vortex, which would inherently be limited to $0 < \Delta z < 0.05$.

To provide further insight the three-dimensional mean flow around the serrations is visualized by plotting fluid variables for y–z planes, skipping every second point in y and z, located at the root of the serrations ($x = 1.00$), halfway along the serrations ($x = 1.06$) and slightly downstream of the serration tips ($x = 1.15$). In order to provide the best-quality data possible, results have also been averaged spatially over the four serrations, before multiplying the data series in the spanwise direction to return the original dimensions of the computational domain. Serration tips are located at $z = 0, 0.05, 0.1, 0.15, 0.2$ and serration roots are located at $z = 0.025, 0.075, 0.125, 0.175$. For the purpose of plotting y–z planes the wall normal velocity is plotted in preference to $\overline{v}$, defined as $\overline{v_n} = u\cos(\alpha) + v\sin(\alpha)$, with $\alpha = 5°$ the aerofoil incidence. This gives a more accurate indication of whether or not there is fluid flow perpendicular to the splitter plate, or 'through' the serrations. In figure 22 the mean velocity components $\overline{v_n}$ and $\overline{w}$ are plotted. At $x = 1.00$ the fluid above the aerofoil possesses negative wall-normal velocity, whilst below the aerofoil the wall-normal velocity is mostly positive, with a very small separated region near the wall.

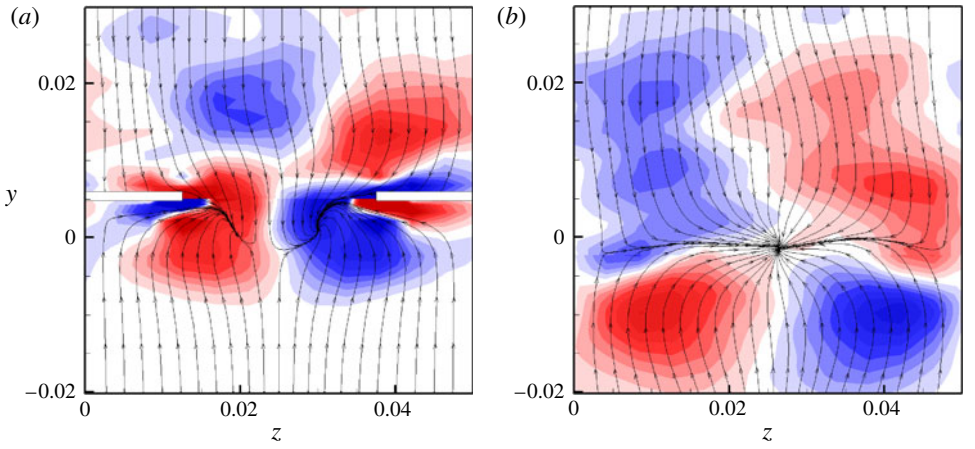

FIGURE 23. (Colour online) Streamlines formulated from the spanwise and wall-normal velocity components at $x = 1.06$ (a) and $x = 1.15$ (b) of the serrated trailing-edge case, also showing contours of streamwise vorticity over the range $\omega_x = \pm 5$.

The effect of the serrations can be observed as a spanwise undulation in the mean flow. Further downstream, at $x = 1.06$, $\overline{v_n}$ remains negative/positive above/below the aerofoil respectively, but it can be seen that between the serrations $\overline{v_n}$ is negative, hence there is a tendency for the upper boundary layer flow to penetrate through the serrations into the lower boundary layer here. On the upper plate surface, at the left- and right-hand edges of the serrations the w-velocity is negative and positive respectively, as the fluid flows downwards and around the serrations. Directly below the flat plate the w-velocity retains the same sign, but further still below the plate (at $y \approx -0.01$) the w-velocity changes sign. This is because the fluid flowing through the serrations is, in the time-average, separating from the underside of the flat plate leading to a small recirculation region. The complexity of the behaviour here is illustrated by plotting streamlines of the $v - w$ velocity components (figure 23). However, it should be noted that since data capture for the y–z planes skips every other point in the y and z directions, the near-wall behaviour is likely to exhibit decreased accuracy, particularly where 'ghost-cells' for the immersed-boundary method are omitted. The downward fluid flow is clearly observed to deflect around the serrations, leading to the presence of counter-rotating streamwise vortices, as well as small separated regions directly below the serrations. By $x = 1.15$ the flow is less complex, consisting of four alternately positive/negative regions of streamwise vorticity, but there is no swirling motion in the mean-flow as there is at $x = 1.06$.

Reynolds stress components and $\overline{p'p'}$ are plotted for y–z planes in figures 24 and 25. Similar to the spanwise averaged statistics illustrated in figure 14, the quantity $\overline{u'u'}$ exhibits unusual behaviour. In the turbulent boundary layer $\overline{u'u'}$ is a maximum at spanwise locations between the serrations; this could be viewed as being because these are the regions where fluid if furthest away from the flat-plate surface (i.e. the no-slip condition). At $x = 1.06$ $\overline{u'u'}$ fluctuations are starting to influence the flow below the splitter plate. The $\overline{u'u'}$ fluctuations behave unusually in that they manifest as discrete maxima located between each serration and slightly below the wake centreline. By $x = 1.15$ this behaviour has become more pronounced, and in fact the $\overline{u'u'}$ fluctuations here are almost as great as for the turbulent flow above the

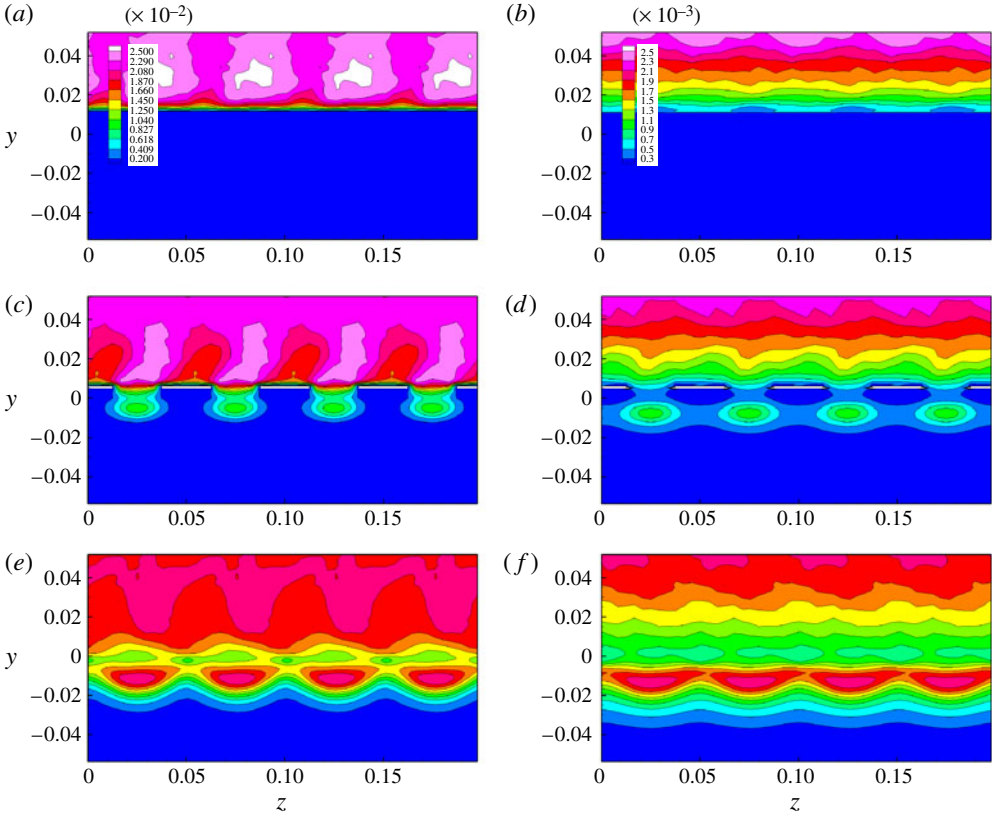

FIGURE 24. (Colour online) Iso-contours of $2 \times 10^{-3} < \overline{u'u'} < 2.5 \times 10^{-2}$ (*a*,*c*,*e*) and $3 \times 10^{-3} < \overline{p'p'} < 2.5 \times 10^{-2}$ (*b*,*d*,*f*) for the serrated trailing-edge case, as computed for *y*–*z* planes at *x*-locations indicated: (*a*) $\overline{u'u'}$ at $x = 1.00$; (*b*) $\overline{p'p'}$ at $x = 1.00$; (*c*) $\overline{u'u'}$ at $x = 1.06$; (*d*) $\overline{p'p'}$ at $x = 1.06$; (*e*) $\overline{u'u'}$ at $x = 1.15$; (*f*) $\overline{p'p'}$ at $x = 1.15$.

wake centreline. Clearly the turbulent flow is not passively convecting through the serrations, as this could not explain the large local magnitudes of $\overline{u'u'}$. It appears that the region of maximum $\overline{u'u'}$ observed in the spanwise averaged statistics (figure 14) for the serrated trailing-edge case is actually due to the presence of a spanwise periodic arrangement of $\overline{u'u'}$ maxima, that are even larger in amplitude than the spanwise averaged statistics would suggest. Furthermore, plotting $\overline{p'p'}$(figure 24*b*,*d*,*f*) illustrates that these *u*-velocity fluctuations cause significant pressure fluctuations in direct vicinity of the trailing edge, and hence could play a role in the production of trailing-edge noise.

The quantity $\overline{v'v'}$ behaves in a simpler fashion. At $x = 1.00$ $\overline{v'v'}$ is significant only above the aerofoil, and is not strongly modified by the presence of serrations. By $x = 1.06$ the fluid between the serrations is subject to increased $\overline{v'v'}$ fluctuations, and by $x = 1.15$ the $\overline{v'v'}$ amplitudes are significant everywhere below the wake dividing line, although $\overline{v'v'}$ remains a maximum in the spaces between serrations. The quantity $\overline{w'w'}$ behaves qualitatively similarly at $x = 1.06$, but the penetration of $\overline{w'w'}$ into the lower wake is significantly slower than $\overline{v'v'}$, presumably because of the orientation of $\overline{v'v'}$ fluctuations with respect to the flat plate. At $x = 1.15$ $\overline{w'w'}$ is a maximum in

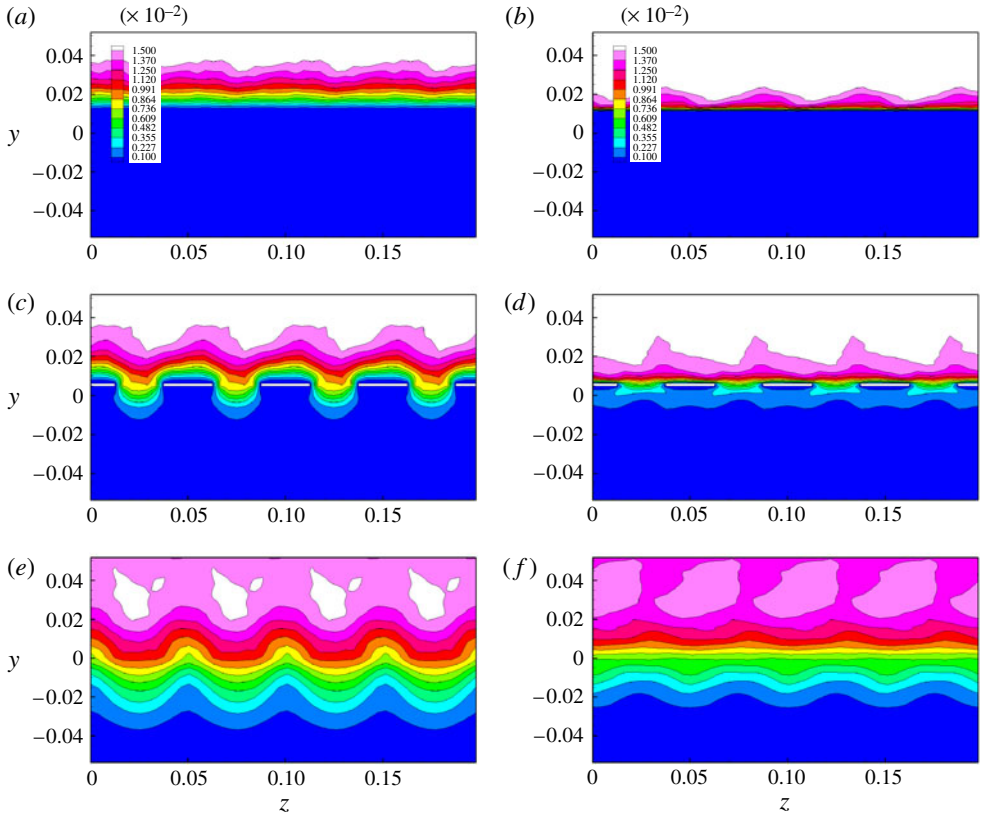

FIGURE 25. (Colour online) Iso-contours of $1 \times 10^{-3} < \overline{v'v'} < 1.5 \times 10^{-2}$ (*a*,*c*,*e*) and $1 \times 10^{-3} < \overline{w'w'} < 3 \times 10^{-2}$ (*b*,*d*,*f*) for the serrated trailing-edge case, as computed for y–z planes at x-locations indicated: (*a*) $\overline{v'v'}$ at $x = 1.00$; (*b*) $\overline{w'w'}$ at $x = 1.00$; (*c*) $\overline{v'v'}$ at $x = 1.06$; (*d*) $\overline{w'w'}$ at $x = 1.06$; (*e*) $\overline{v'v'}$ at $x = 1.15$; (*f*) $\overline{w'w'}$ at $x = 1.15$.

line with the serration tips, which contrasts with the $\overline{v'v'}$ fluctuations, which are a maximum aligned with the spaces between serrations, although the degree of spanwise variation is less for $\overline{w'w'}$. This behaviour appears to corroborate the observation that horseshoe vortices form between the serrations. If the serrations are responsible for the development of horseshoe vortices, the 'legs' of the vortex would be aligned with the serration tips, whilst the loop of the vortex would be located in the space between serrations. Since streamwise vorticity is dominant in the legs of the vortex, v' and w' fluctuations would be expected to dominate here. Conversely, at the loop of the vortex spanwise vorticity would be expected to dominate, corresponding to u' and v' fluctuations. The fact that $\overline{u'u'}$ and $\overline{v'v'}$ are a maximum between the serrations, whilst $\overline{w'w'}$ is a maximum aligned with the serration tips, supports this hypothesis. The mean flow through the serrations appears to generate regions of positive (anticlockwise) and negative (clockwise) streamwise vorticity directly below the serrations, however, whereas the horseshoe vortices observed in Q-plots exhibit an opposite negative/positive pattern. Nevertheless, it has been observed that a small recirculation region exists below the serrations, and that the w-velocity (and ω_x) is large here. It is likely that the horseshoe vortices form when a local gust or eddy

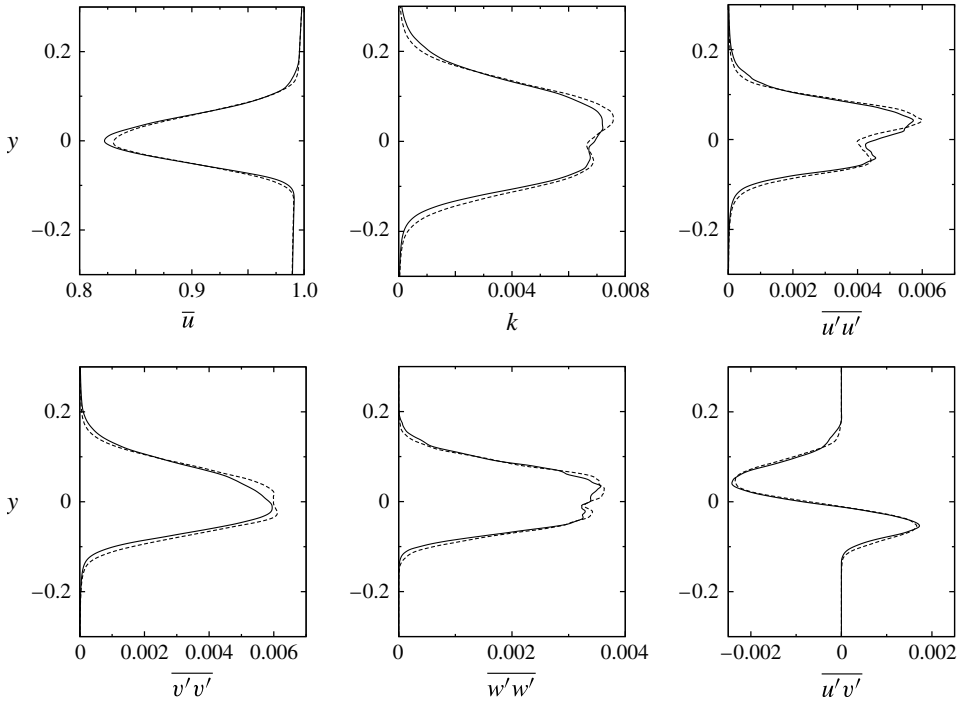

FIGURE 26. Time-averaged and spanwise averaged velocity quantities recorded in the wake at $x = 2$ for the straight (—) and serrated (- - -) trailing-edge cases.

convects through the space between serrations. It seems feasible that under such circumstances the recirculation region could grow in size and promote the formation of a horseshoe vortex with the same sign as those observed here. Animations of Q illustrate the horseshoe legs ending by touching the lower serration edges, as opposed to being divorced from the plate surface, providing circumstantial evidence that the recirculation region may indeed be responsible for the formation of the horseshoe vortices.

It appears therefore that trailing-edge serrations can affect the formation of turbulent structures in the direct vicinity of the trailing edge itself. This is important in terms of aerofoil self-noise, since the production of vortical structures at a trailing edge can be a noise source in itself (i.e. trailing-edge bluntness noise). It appears likely that at increased incidence (or higher loading) the disparity between upper and lower boundary layer properties will increase, as well as the fluid flow through the serrations, promoting such behaviour.

5.5. *Behaviour in the wake*

The structure of the aerofoil wake is of interest for situations where wake impingement may occur, for example in multiple-turbine flows (both for propulsion and energy production, e.g. in 'wind farms'), hence it is important to determine whether the presence of trailing-edge serrations modifies the structure of the wake. Mean velocity, turbulent kinetic energy and Reynolds stress components are plotted in figure 26 at a distance one chord downstream of the aerofoil trailing edge (i.e. $x = 2.0$). The serrated trailing-edge case exhibits a slightly smaller velocity deficit in the centre of

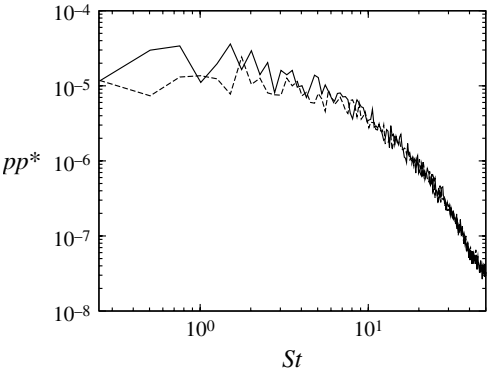

FIGURE 27. Pressure spectra computed in the wake at $(x, y) = (2, 0)$ for the straight (—) and serrated (- - -) trailing-edge cases.

the wake, in conjunction with a larger maximum amplitude turbulent kinetic energy, with both peaks in turbulent kinetic energy being slightly larger in amplitude than for the straight trailing-edge case. Although subtle, the trend is to a slightly faster wake, with greater turbulent intensity. The Reynolds stress components broadly follow similar distributions for both cases, with some differences in peak-amplitude, the exception being $\overline{v'v'}$, for which the serrated trailing-edge case exhibits a broader double-peak distribution.

Pressure spectra recorded at $(x, y) = (2, 0)$ show that above $St = 10$ both flows exhibit similar frequency content. Below $St = 10$ the straight trailing-edge case exhibits greater amplitude; however, this appears to contradict the statistics plotted in figure 26, which suggest greater turbulent kinetic energy for the serrated trailing-edge case. On inspection it appears that at $y = 0$ the turbulent kinetic energy is actually larger for the straight trailing-edge case than for the serrated case (figure 26*b*), and this is reflected in the spectra. Since the ensemble-averaged statistics plotted in figure 26 will be dominated by high-energy, low-frequency events, it is hypothesized that were the spectra recomputed for a location where the turbulent kinetic energy is larger for the serrated trailing-edge case, the spectra would correspondingly exhibit greater energy at low frequencies. Spanwise correlations within the wake can be compared by referring back to figures 18–21, where a dashed box is plotted for comparison purposes at $x \approx 2$. Differences between the straight and serrated trailing-edge cases are not as pronounced as for the near trailing-edge region. However, it can be surmised that for the serrated trailing-edge case at $x \approx 2$ spanwise correlation levels are marginally decreased for $2 < St < 5$ and $5 < St < 10$, and marginally increased for $10 < St < 15$ and $20 < St < 25$. To summarize, although differences between the two wakes can be observed at $x = 2$, the differences are slight and likely to become less significant with increasing downstream distance.

6. Conclusions

Direct numerical simulations have been performed of the low Reynolds-number flow around a NACA-0012 aerofoil with the addition of a flat-plate trailing-edge extension. Two cases were conducted in total, consisting of serrated and straight trailing-edge splitter plates. The flow topology is complex, with a laminar separation bubble present on the upper aerofoil surface, which reattaches as a turbulent boundary

layer, leading to noise production in the vicinity of transition/reattachment as well as the trailing-edge noise investigated here. The presence of the trailing-edge serrations is found to significantly reduce the amplitude of the trailing-edge noise for all frequencies above an onset Strouhal number of $St \approx 5$. Neither the directivity or spanwise correlation levels of the acoustic radiation appear to change significantly for frequencies where the noise reduction is prominent. Analysis of the upper surface boundary layer illustrates that the flow upstream of the aerofoil trailing edge is similar for the serrated and straight trailing-edge cases, including Reynolds stress amplitudes, turbulent spectra and spanwise correlation levels. This implies that changes in the sound radiation are caused solely by changes to the scattering process itself, and potentially by changes to the hydrodynamic behaviour in the direct vicinity of the serrations.

Hydrodynamic differences between the two flows appear strongest in the vicinity of the trailing edge; further downstream, within the aerofoil wake, differences between the two flows are slight, hence the presence of serrations is likely to have little bearing on flows where wake impingement is important. Considering the ratio of streamwise to spanwise pressure derivatives reveals that the turbulent structures are predominantly orientated in the streamwise direction, but that spanwise gradients are dominant in direct vicinity of the straight trailing edge, evidencing the trailing-edge discontinuity. This behaviour is not apparent for the serrated trailing-edge case, where the streamwise orientated turbulent structures more smoothly graduate to a spanwise dominated regime as they convect over the trailing edge. Three-dimensional plots of vortical structures suggest that the serrated trailing edge prevents the passage of turbulent structures with large spanwise extent, and illustrates the tendency for horseshoe vortices to form in the spaces between serrations and to convect into the wake. These horseshoe vortices possess opposite sign streamwise vorticity to that observed in the mean flow, and appear responsible for large values of $\overline{u'u'}$ located downstream of the trailing edge, aligned with the spaces between serrations. Spanwise correlations computed in the vicinity of the trailing edge are consistent with this observation, exhibiting increased levels of correlation, most significantly for spanwise separations up to one serration wavelength. It appears likely that the formation of these vortices is exacerbated by the presence of a mean downward (negative v) velocity through the serrations, and that an increase in aerofoil incidence may lead to more regular horseshoe vortex production and/or with greater vorticity intensity.

Acknowledgement

This work was supported by EPSRC grant EP/F048017/1.

REFERENCES

AMIET, R. K. 1976 Noise due to turbulent flow past a trailing edge. *J. Sound Vib.* **47** (3), 387–393.

BROOKS, T. F., POPE, D. S. & MARCOLINI, M. A. 1989 *Airfoil Self-Noise and Prediction*. NASA Reference Publication 1218, NASA.

CALLENDER, B., GUTMARK, E. & MARTENS, S. 2005 Far-field acoustic investigation into chevron nozzle mechanisms and trends. *AIAA J.* **43** (1), 87–95.

CARPENTER, M. H., NORDSTRÖM, J. & GOTTLIEB, D. 1999 A stable and conservative interface treatment of arbitrary spatial accuracy. *J. Comput. Phys.* **148** (2), 341–365.

FFOWCS WILLIAMS, J. E. & HALL, L. H. 1970 Aerodynamic sound generation by turbulent flow in the vicinity of a scattering half plane. *J. Fluid Mech.* **40** (4), 657–670.

GRUBER, M. & JOSEPH, P. F. 2011 On the mechanisms of serrated aerofoil trailing edge noise reduction. In *17th AIAA/CEAS Aeroacoustics Conference, Portland, Oregon, June*. AIAA.

HEAD, M. R. & BANDYOPADHYAY, P. 1981 New aspects of turbulent boundary-layer structure. *J. Fluid Mech.* **107**, 297–338.

HERR, M. & DOBRZYNSKI, W. 2005 Experimental investigations in low-noise trailing-edge design. *AIAA J.* **43** (6), 1167–1175.

HOWE, M. S. 1991 Noise produced by a sawtooth trailing edge. *J. Acoust. Soc. Am.* **90**, 482.

JONES, L. E. 2007 Numerical studies of the flow around an aerofoil at low Reynolds number. PhD thesis, University of Southampton.

JONES, L. E., SANDBERG, R. S. & SANDHAM, N. D. 2008 Direct numerical simulations of forced and unforced separation bubbles on an aerofoil at incidence. *J. Fluid Mech.* **602**, 175–207.

JONES, L. E., SANDBERG, R. D. & SANDHAM, N. D. 2009 Investigation and prediction of transitional airfoil self-noise. In *AIAA Paper* 2009–3104, *15th AIAA/CEAS Aeroacoustics Conference, Miami, May*. AIAA.

JONES, L. E., SANDBERG, R. S. & SANDHAM, N. D. 2010*a* Stability and receptivity characteristics of a laminar separation bubble on an aerofoil. *J. Fluid Mech.* **648**, 257–296.

JONES, L. E., SANDHAM, N. D. & SANDBERG, R. D. 2010*b* Acoustic source identification for transitional aerofoil flows using cross correlations. *AIAA J.* **48** (10), 2299–2312.

LIGHTHILL, M. J. 1952 On sound generated aerodynamically. Part 1. General theory. *Proc. R. Soc. Lond. Ser.* A: *Math. Phys. Sci.* **211A** (1107), 564–587.

MITTAL, R. & IACCARINO, G. 2005 Immersed boundary methods. *Annu. Rev. Fluid Mech.* **37**, 239–261.

OERLEMANS, S., FISHER, M., MAEDER, T. & KÖGLER, K. 2009 Reduction of wind turbine noise using optimized aerofoils and trailing-edge serrations. *AIAA J.* **47** (6), 1470–1481.

SANDBERG, R. D. & JONES, L. E. 2011 Direct numerical simulations of low Reynolds number flow over aerofoils with trailing-edge serrations. *J. Sound Vib.* **330**, 3818–3831.

SANDBERG, R. D., JONES, L. E. & SANDHAM, N. D. 2008 Direct numerical simulations of noise generated by turbulent flow over aerofoils. *AIAA Paper* 2008–2861, *14th AIAA/CEAS Aeroacoustics Conference, Vancouver, Canada*. AIAA.

SANDBERG, R. D. & SANDHAM, N. D. 2006 Nonreflecting zonal characteristic boundary condition for direct numerical simulation of aerodynamic sound. *AIAA J.* **44** (2), 402–405.

SANDHAM, N. D., LI, Q. & YEE, H. C. 2002 Entropy splitting for high-order numerical simulation of compressible turbulence. *J. Comput. Phys.* **178**, 307–322.

WHITE, F. M. 1991 *Viscous Fluid Flow*. McGraw-Hill.